Applied Physics Letters

Dealloying-induced phase transformation in Fe–Rh alloys

Cite as: Appl. Phys. Lett. **120**, 141904 (2022); https://doi.org/10.1063/5.0088048
Submitted: 12 February 2022 • Accepted: 30 March 2022 • Published Online: 08 April 2022

Xinglong Ye, Holger Geßwein, Di Wang, et al.

Applied Physics Letters ARTICLE scitation.org/journal/apl

Dealloying-induced phase transformation in Fe–Rh alloys

Cite as: Appl. Phys. Lett. **120**, 141904 (2022); doi: 10.1063/5.0088048
Submitted: 12 February 2022 · Accepted: 30 March 2022 ·
Published Online: 8 April 2022

Xinglong Ye,[1,a)] Holger Geßwein,[2] Di Wang,[1,3] Askar Kilmametov,[1] Horst Hahn,[1] and Robert Kruk[1]

AFFILIATIONS

[1]Institute of Nanotechnology, Karlsruhe Institute of Technology, 76344 Eggenstein-Leopoldshafen, Germany
[2]Institute for Applied Materials, Karlsruhe Institute of Technology, 76344 Eggenstein-Leopoldshafen, Germany
[3]Karlsruhe Nano Micro Facility, Karlsruhe Institute of Technology, 76131 Karlsruhe, Germany

[a)]Author to whom correspondence should be addressed: xing-long.ye@kit.edu

ABSTRACT

Nanoporous metals produced by dealloying have aroused enormous interest due to exotic mechanical and physico-chemical properties that are usually inaccessible in their bulk form. Interestingly, when binary solid-solution alloys, such as Ag–Au alloys, are dealloyed, the resulting nanoporous metals usually inherit the crystal structure of their parent alloys. In this Letter, we examined the evolution of the crystal structure during the dealloying of Fe–Rh alloys that show single-phase solubility over a large range of compositions. *In situ* x-ray diffraction shows that the crystallographic structure of the $Fe_{85}Rh_{15}$ alloy transforms from the original *bcc* to *fcc* structure during the dealloying. Transmission electron microscopy confirms the *fcc* structure of the nanoporous sample, which exhibits a typical bi-continuous porous structure with ligament sizes of only 2–3 nm and a high Fe concentration. The *bcc–fcc* transformation is driven by the chemical disordering of Fe and Rh atoms, induced by the highly dynamic dissolution and diffusion process at the alloy/electrolyte interface. Our study highlights the massive diffusion and the consequent disordered arrangement of elemental components during the evolution of the nanoporous structure.

Dealloying is a corrosion process that selectively dissolves one or more elemental components with relatively low electronegativity in an alloy. It has recently emerged as a powerful approach for fabricating nanoporous (NP) metals, which exhibit an open porous morphology with inter-penetrating ligaments and pores at the nanometer scale.[1,2] Due to their extremely large surface area, they can feature mechanical and physico-chemical properties that are inaccessible in bulk metals such as ultrahigh specific strength,[3,4] "piezo-electric" effect,[5,6] responsive strength,[7,8] and high catalytic activity.[9,10] With their overall monolithic form, NP metals also offer an extremely versatile platform to unveil hidden physical properties resulting from the strong surface effects.[11,12]

The evolution of nanoporosity can theoretically be described by the working model that involves the selective dissolution and surface diffusion processes.[13–15] As exemplified in the prototypical Ag–Au alloy, Ag atoms are selectively dissolved from atomic terraces, and the Au atoms remain during the dealloying, which produces the supersaturated solution of Au ad-atoms and vacancies at the alloy/electrolyte interface. Being thermodynamically unstable, this supersaturated solution decomposes into a two-phase structure of Au clusters and pores through uphill diffusion, leading eventually to the porous structure.[13] On the other hand, from the experimental point of view, substantial efforts have been devoted to characterize the morphology of the resultant NP structure, especially with regard to the ligament sizes and contents of residual Ag. The observed ligament sizes span from a few nanometers to sub-micron scale[16,17] and the residual Ag concentration from 0 to 70 at. %.[18,19] This large-range scale arises from the secondary coarsening/dealloying process that occurs behind the corrosion front, which can complicate the direct comparison of experimental results with the theoretical predictions.

The understanding of the nanoporosity formation requires, among others, the investigation of the evolution of the crystal structure during the dealloying. When the solid-solution alloys are dealloyed, the formed NP samples usually inherit the crystal structure and orientation of their parent alloys, for instance, in Au–Ag alloys.[20,21] This is expected from the dissolution/surface diffusion model since the single-phase solubility allows the composition to change continuously within the same crystal structure. In contrast, the dealloying of stoichiometric intermetallic compounds and amorphous alloys often induces the change in the crystal structure. The selective removal of the less noble

elements breaks the proportions of two elements required for strict stoichiometry in intermetallic compounds[22–24] and in amorphous alloys undermines the glass-forming stability.[25–32]

In this Letter, we investigated the evolution of the crystal structure during the dealloying of the Fe–Rh alloy, which exhibits a single body-centered-cubic (*bcc*) phase with extended Rh solubility up to ∼50 at. % Rh.[33] However, we found that the *bcc* structure transforms to the face-centered-cubic (*fcc*) structure during the dealloying although the composition of the obtained NP sample still resides in the region of the *bcc* phase. The obtained NP Rh(Fe) samples have extremely small ligament sizes of only 2–3 nm and the retention of 60 at. % Fe, evidencing the stability of the NP structure against secondary coarsening. These findings were discussed within the framework of the dissolution/surface diffusion model, considered with the chemical disordering induced by the massive transfer of both elements during the dealloying.

We used the Fe–Rh alloy with a nominal composition of 85 Fe:15 Rh (at. %) as the parent alloy for the electrochemical dealloying. The alloy ingots were prepared by repetitive arc melting of Fe and Rh wires (>99.99%) in an Ar atmosphere. They were first homogenized at 1000 °C for four days, compressed, and finally cut into millimeter-sized samples. Cold rolling was further used to prepare thin-sheet samples with a reduced thickness of ∼0.12 mm for *in situ* x-ray diffraction (XRD) measurements. All samples were annealed at 850 °C to remove residual stress before the electrochemical dealloying. In both annealing steps, the samples were slowly cooled in the furnace that stabilized the samples in their equilibrium *bcc* phases. We used a three-electrode electrochemical system to characterize the anodization behavior and performed the electrochemical dealloying of the alloy samples in 1M H_2SO_4 under potentiostatic control (Autolab PGSTAT302N). The working, counter, and reference electrodes were $Fe_{85}Rh_{15}$ samples, Pt wires, and a pseudo Ag/AgCl electrode, respectively. The pseudo Ag/AgCl reference electrode was prepared by anodizing an Ag wire upon application of 1 V against another Ag wire in 1 M HCl for 60 s. The potential of this peudo Ag/AgCl electrode was 0.420 ± 0.002 V more positive than the standard Hg/HgO (6M KOH) electrode, and for comparison, all the voltages in the paper were converted to the Hg/HgO scale. *In situ* x-ray diffraction was conducted to track the structural evolution with a parallel beam laboratory rotating anode diffractometer (Mo $K_{\alpha1,\alpha2}$ radiation). The 2D diffraction images were integrated by pyFAI software and analyzed with the Rietveld method (TOPAS V6). NIST SRM660b LaB_6 powders were used for the detector calibration and the determination of the instrumental resolution. The microstructures of NP Fe(Rh) samples were characterized by transmission electron microscopy (TEM, FEI Titan 80-300) and scanning electron microscopy (SEM, Zeiss Ultra 600). When exposed to air, the as-prepared NP samples were very prone to oxidation due to the large amount of chemically active Fe elements and the nanometer-scale ligaments. To avoid the oxidation during preparation of a TEM specimen, we ground the NP samples to fine powders inside a glovebox under argon protection, from where a vacuum-transfer TEM holder, containing the ground powder, can then be directly transferred to the TEM chamber for further observation. The residual Fe contents were measured by energy dispersive spectroscopy on the cross section of NP samples in a SEM chamber.

We first studied the electrochemical behavior of the $Fe_{85}Rh_{15}$ alloy in 1 M H_2SO_4. As shown in Fig. 1, the anodic polarization curve reveals the existence of the critical dealloying potential ($E_{critical}$) and

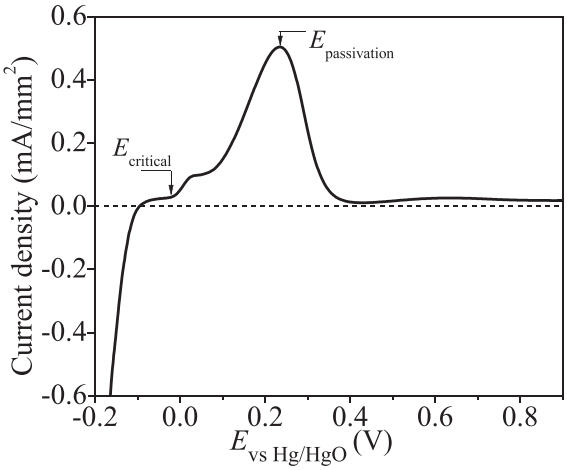

FIG. 1. An anodic polarization curve of the $Fe_{85}Rh_{15}$ alloy in 1 M H_2SO_4, showing the existence of the critical dealloying potential and the passivation potential. $E_{critical}$ refers to the critical dealloying potential at −0.020 V, above which the current increases exponentially and the bulk dealloying can proceed. $E_{passivation}$ refers to the potential of 0.235 V, where the current drops drastically due to the passivation with Rh oxide. The scanning rate is 2 mV/s.

the passivation potential ($E_{passivation}$). As indicated by the arrow, $E_{critical}$ is at around −0.02 V, above which the current starts to increase exponentially, indicating the onset of the bulk dealloying. The existence of the critical dealloying potential has been observed in other binary solid-solution alloy systems such as the Ag–Au alloy.[34,35] A series of chronoamperometry curves measured at different constant potentials around -0.02 V, which follows the procedures in Ref. 36, show that the dealloying can proceed at the lowest potential of −0.020 V. However, unlike in the case of the Au–Ag alloy, the dealloying current drops drastically at 0.23 V, referred to as the passivation potential. This arises from the formation of Rh oxide that prevents the exposure of the pristine alloy to the electrolyte, a phenomenon also observed in the dealloying of the Cu–Rh alloy.[37] Consequently, the potentials from −0.020 V to about 0.23 V can be used to perform the electrochemical dealloying of $Fe_{85}Rh_{15}$ alloys. Based on our previous study,[19] we chose the dealloying potential that is slightly higher than $E_{critical}$, here −0.015 V, for the electrochemical dealloying of $Fe_{85}Rh_{15}$ alloys. It minimized the influence of the secondary dealloying process and preserved the initial NP structure.

Figure 2(a) shows the evolution of the crystal structure of the $Fe_{85}Rh_{15}$ alloy during the dealloying at −0.015 V by *in situ* XRD in transmission geometry. The transmission geometry allows the detection of the entire volume of the sample rather than only its surface (thickness ∼0.1 mm). At the beginning, the XRD pattern shows the typical *bcc* structure at room temperature. As the dealloying was commenced by applying −0.015 V, the intensity of *bcc* diffraction peaks decreased gradually and disappeared after ∼5 h. Meanwhile, another set of diffraction peaks appeared, which can be ascribed to an *fcc* structure. After about 10 h, the intensity of the newly-developed *fcc* pattern remained stable, indicating the completeness of the dealloying process. Figure 2(b) shows the diffraction patterns at three different stages of the dealloying process, i.e., the pristine alloy, the partially dealloyed sample, and the sample after the complete dealloying. It is clear that

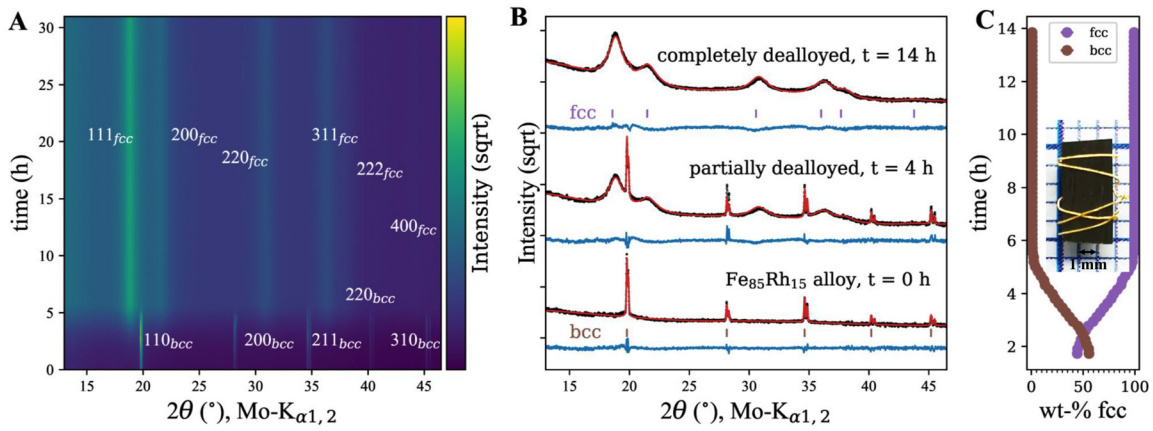

FIG. 2. (a) A contour plot of *in situ* x-ray diffraction patterns during the dealloying of the $Fe_{85}Rh_{15}$ alloy at −0.015 V, showing the phase transformation from the original *bcc* to *fcc* structure. (b) Rietveld fitting of the diffraction patterns at different stages of the dealloying process, i.e., the pristine alloy, the partially dealloyed sample, and the completely dealloyed sample. Note the significant peak broadening due to the formation of the NP structure. (c) The linear change in the weight fraction of the *fcc* and *bcc* phases during the dealloying, verifying the constant dealloying rate. Inset shows the photo of the NP sample with a thin-sheet form.

after the complete dealloying, the diffraction peaks exhibit significant broadening, indicating the extremely small coherent diffraction domains, most likely the ligaments, and the presence of large micro-strains. The contribution of the apparent grain size (D) and the micros-train (ε) to peak broadening can usually be decoupled by Williamson–Hall analysis, i.e., $\beta\cos\theta = K\lambda/D + 4\varepsilon\sin\theta$, in which β, K, and λ are the integral width, Scherrer constant, and x-ray wavelength, respectively. Yet, a striking feature is the deviation of the Bragg peak positions from the ideal *fcc* structure, i.e., the 200_{fcc} peak is shifted to lower diffraction angles. These features indicate the existence of the anisotropic strain and/or stacking faults.[38] The observed diffraction pattern resembles that of an expanded austenite,[39] whose crystal structure can be approximated with a faulted *fcc* structure and anisotropic distortions.[40] To account for both the relative displacement between 111_{fcc} and 200_{fcc} and the peak broadening, we used an elastic anisotropy factor for cubic materials, which describes the anisotropic distortion[41] and the anisotropic peak broadening model with fitting parameters of S_{400} and S_{220}.[42] Rietveld analysis shows that the ligament sizes are only about 3 nm. The refined anisotropic strain coefficients S_{400} and S_{220} indicate that the variance of the lattice parameters is largest in the [100] directions and smallest in the [111] directions with maximum micro-strain values of 0.8% and 0.3%, respectively. The micro-strain is much larger than that observed in NP Au with ligament sizes of ∼20 nm, which can result from the extremely small ligament sizes, due to which surface stress generates large stress and strain in the ligaments.[43] It is worthwhile to note that the large micro-strain with anisotropic distortion leads to the co-existence of spin glass and ferromagnetic ground states in NP FeRh.[44]

Figure 2(c) shows the change of the weight fractions of the *bcc* and *fcc* phases during the dealloying, which were obtained from the Rietveld fitting of the diffraction patterns during the dealloying [Fig. 2(b)]. Obviously, the fraction of the original *bcc* phase decreases linearly with the dealloying time, and correspondingly, the fraction of the *fcc* phase changes reversely. This linear change of phase fraction arises from the thin-sheet form of the $Fe_{85}Rh_{15}$ alloy as shown in the inset of Fig. 2(c) due to which the dealloying proceeds along the out-of-plane direction with a constant rate. Our *in situ* XRD results, thus, clearly reveal the phase transformation of the $Fe_{85}Rh_{15}$ alloy from the *bcc* to *fcc* structure during the dealloying.

We performed TEM to examine the microstructure of the NP Rh(Fe) samples. Figure 3(a) shows the typical NP morphology with interpenetrating ligaments and pores. The enlarged TEM images reveal the extremely small ligament sizes of only 2–3 nm, which evidences the suppression of the secondary coarsening during the dealloying [Fig. 3(b)]. The stabilization of the NP structure against coarsening results from the low surface diffusivity of Rh atoms, which plays the similar role as that of Pt atoms in Au(Pt)–Ag alloys.[19,45] The corresponding selected area diffraction shows continuous diffraction rings, indicating the nearly randomly distributed nano-grains with the *fcc* structure [the inset in Fig. 3(b)]. Moreover, energy dispersive spectroscopy shows that the Fe concentration increases monotonically with the lower dealloying potentials and reaches up to ∼60 at. % Fe at −0.015 V [Fig. 3(c)]. The retention of the high concentration of Fe elements is similar to that observed in the Pt-doped NP Au samples, in which 65 at. % Ag was observed when the secondary coarsening/dealloying was suppressed as well.[19] We emphasize that the extremely small ligament sizes and the high concentration of residual Fe elements signify the preservation of the initial NP structure created by dealloying. Hence, the observed *bcc–fcc* transformation originates from the primary dealloying process rather than other secondary processes that occur behind the corrosion front. It is also worthwhile to note that the *bcc–fcc* phase transformation was observed in NP Fe(Rh) prepared by the dealloying at −0.005, 0.010, and 0.030 V, with Fe concentrations ranging from ∼50 at. % to 20 at. %.

Our *in situ* XRD and TEM results show the *bcc–fcc* transformation during the dealloying of the $Fe_{85}Rh_{15}$ alloy.

Figure 4 shows that similar to Au–Ag alloys, Fe–Rh alloys have the single phase structure with the extended Rh solubility up to ∼50 at. %.[33] Since the composition of NP Fe(Rh) is ∼60 at. % Fe, which still resides in the *bcc* region, one may expect NP Fe(Rh) to retain the *bcc* structure of the parent alloy (arrow in Fig. 4). Instead, we observed the phase transformation from the *bcc* to *fcc* structure. In

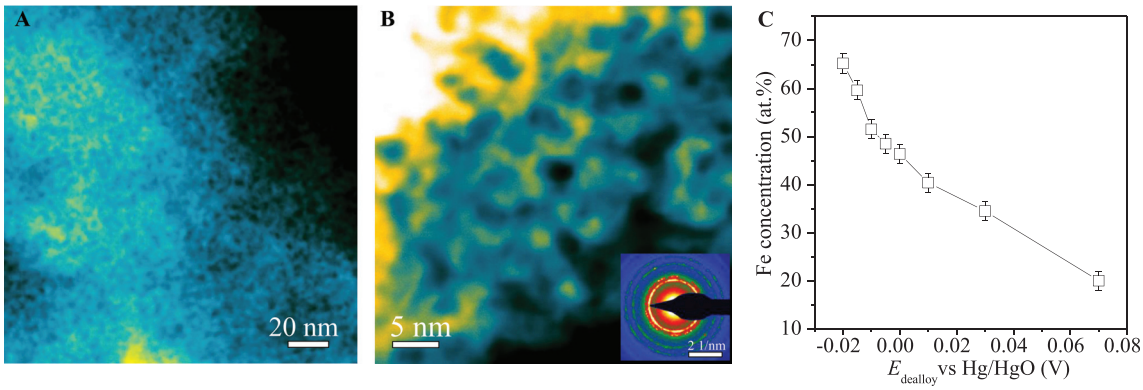

FIG. 3. (a) A bright-field TEM image showing the typical NP morphology with bi-continuous ligaments and pores. (b) The enlarged view of the NP morphology exhibiting a mean ligament size of only 2–3 nm. (Inset) The corresponding selected area diffraction patterns confirming the *fcc* structure. (c) The dependence of Fe concentrations on the dealloying potentials ($E_{dealloy}$).

fact, as mentioned earlier, the resultant NP structure inherits the *fcc* structure of the parent alloys in the dealloying of Ag–Au alloys.[20,21] However, it should be noted that Au–Ag alloys show the single-phase solubility with the *fcc* structure across all temperatures and compositions, allowing for the continuous change in composition within the same crystal structure. However, in the case of the Fe–Rh alloy, there exists the phase transformation from the *bcc* to the *fcc* structure at high temperatures, where chemical disordering of Fe and Rh atoms is introduced. The chemical order indicates the occupation of the body-centered sites by one kind of element and the corner sites by another kind, while chemical disordering introduces anti-site defects. It has been observed that the *bcc–fcc* phase transformation in Fe–Rh alloys can be triggered by the chemical-disordering process, for instance, by intensive ball milling.[46,47] This means the *bcc* structure is the thermodynamically stable phase but can be converted to the metastable *fcc* structure when chemical disorder is introduced.

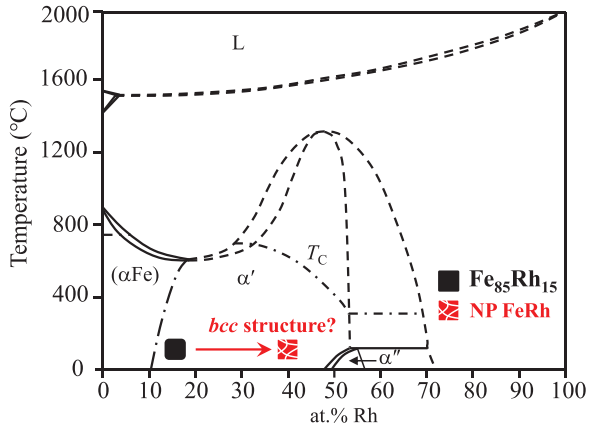

FIG. 4. Phase diagram of the Fe–Rh alloy showing the single-phase solid solubility up to ~50 at. % Rh within the *bcc* structure. After the dealloying, the resultant NP Fe(Rh) is expected to have a *bcc* structure when the Rh concentration is below 50 at. %. However, the *bcc–fcc* transformation was observed although the resultant NP Fe(Rh) still retained 60 at. % Fe.

The observed phase transformation can be interpreted within the framework of the dissolution/surface diffusion model. Based on the working model proposed by Erlebacher and Sierazki, the dealloying process is dominated by the selective dissolution and surface diffusion of remaining elements.[13–15] In our case, Fe atoms are selectively dissolved during the dealloying of the $Fe_{85}Rh_{15}$ alloy, while the remaining Rh and residual Fe atoms will diffuse along the alloy/electrolyte interface. The dissolution and surface diffusion processes can be highly dynamic and non-equilibrium, which will cause the disordered arrangement of Fe and Rh atoms at the alloy/electrolyte interface. The newly formed Fe–Rh clusters with the disordered arrangement of Fe and Rh atoms, thus, tend to form a metastable *fcc* structure rather than the equilibrium *bcc* structure. Consequently, the observed *bcc–fcc* transformation is driven by the chemical disordering of Fe and Rh atoms, as introduced by the highly dynamic dissolution and diffusion process. It is worthwhile to consider that due to the extremely small ligaments, surface stress may deform the ligaments immediately after their formation and even induce phase transformation. In this regard, the *fcc* structure is equivalent to a body-centered-tetragonal (*bct*) structure with $c/a = \sqrt{2}$. Therefore, along the Bain path from *bcc* to *bct*, a tetragonal distortion of 41.4% would be required,[48] which is unlikely to happen in the considered case.

In summary, we studied the evolution of the crystal structure during the dealloying of Fe–Rh alloys that exhibit single-phase solubility up to 50 at. % Rh. We found that the crystal structure transforms from the original *bcc* to the *fcc* one during the dealloying. The resultant NP samples have extremely small ligament sizes of only 2–3 nm and the retention of a high Fe concentration of 60 at. %, which evidence the suppression of secondary coarsening/dealloying processes. The dealloying-induced phase transformation can be attributed to the disordered arrangement of Fe and Rh atoms, which is induced by the highly dynamic dissolution and surface diffusion processes at the alloy-electrolyte interface. Our study can sharpen the understanding of the spontaneous evolution process of nanoporosity and contribute to the development of novel NP metals.

X.Y. would like to thank the Alexander von Humboldt Foundation. We acknowledge support by the KIT-Publication Fund of the Karlsruhe Institute of Technology.

AUTHOR DECLARATIONS

Conflict of Interest

The authors have no conflicts to disclose.

DATA AVAILABILITY

The data that support the findings of this study are available within the article.

REFERENCES

[1]I. McCue, E. Benn, B. Gaskey, and J. Erlebacher, "Dealloying and dealloyed materials," Annu. Rev. Mater. Res. **46**, 263–286 (2016).
[2]J. Weissmüller, R. Newman, H. J. Jin, A. Hodge, and J. Kysar, "Nanoporous metals by alloy corrosion: Formation and mechanical properties," MRS Bull. **34**, 577–586 (2009).
[3]C. A. Volkert, E. T. Lilleodden, D. Kramer, and J. Weissmüller, "Approaching the theoretical strength in nanoporous Au," Appl. Phys. Lett. **89**, 061920 (2006).
[4]X. L. Ye and H. J. Jin, "Strengthening by corrosion: Development of high strength nanoporous metals," Adv. Eng. Mater. **18**, 1050–1058 (2016).
[5]J. Weißmüller, R. N. Viswanath, D. Kramer, P. Zimmer, R. Würschum, and H. Gleiter, "Charge induced reversible strain in a metal," Science **300**, 312–315 (2003).
[6]J. Biener, A. Wittstock, L. Zepeda-Ruiz *et al.*, "Surface-chemistry-driven actuation in nanoporous gold," Nat. Mater. **8**, 47–51 (2009).
[7]H. J. Jin and J. Weißmüller, "A material with electrically tunable strength and flow stress," Science **332**, 1179 (2011).
[8]X. L. Ye, L. Z. Liu, and H. J. Jin, "Responsive nanoporous metals: Recoverable modulations on strength and shape by watering," Nanotechnology **27**, 325501 (2016).
[9]A. Wittstock, V. Zielasek, J. Biener, C. M. Friend, and M. Baeumer, "Nanoporous gold catalysts for selective gas-phase oxidative coupling of methanol at low temperature," Science **327**, 319 (2010).
[10]T. Fujita, P. Guan, K. McKenna *et al.*, "Atomic origins of the high catalytic activity of nanoporous gold," Nat. Mater. **11**, 775–780 (2012).
[11]Y. Y. Zhang, H. Xie, L. Z. Liu, and H. J. Jin, "Surface triple junctions govern the strength of a nanoscale solid," Phys. Rev. Lett. **126**, 235501 (2021).
[12]T. Fujita, H. Okada, K. Koyama *et al.*, "Unusually small electrical resistance of three-dimensional nanoporous gold in external magnetic fields," Phys. Rev. Lett. **101**, 166601 (2008).
[13]J. Erlebacher, M. J. Aziz, A. Karma, N. Dimitrov, and K. Sieradzki, "Evolution of nanoporosity in dealloying," Nature **410**, 450–453 (2001).
[14]J. Erlebacher, "An atomistic description of dealloying—Porosity evolution, the critical potential, and rate-limiting behavior," J. Electrochem. Soc. **151**, C614–C626 (2004).
[15]J. Erlebacher and K. Sieradzki, "Pattern formation during dealloying," Scr. Mater. **49**, 991–996 (2003).
[16]L. H. Qian and M. W. Chen, "Ultrafine nanoporous gold by low-temperature dealloying and kinetics of nanopore formation," Appl. Phys. Lett. **91**, 083105 (2007).
[17]A. Dursun, D. V. Pugh, and S. G. Corcoran, "Dealloying of Ag–Au alloys in halide-containing electrolytes: Affect on critical potential and pore size," J. Electrochem. Soc. **150**, B355 (2003).
[18]Y. Liu, S. Bliznakov, and N. Dimitrov, "Factors controlling the less noble metal retention in nanoporous structures processed by electrochemical dealloying," J. Electrochem. Soc. **157**, K168 (2010).
[19]X. L. Ye, N. Lu, X. J. Li, K. Du, J. Tan, and H. J. Jin, "Primary and secondary dealloying of Au(Pt)–Ag: Structural and compositional evolutions, and volume shrinkage," J. Electrochem. Soc. **161**, C517–C526 (2014).
[20]H. J. Jin, L. Kurmanaeva, J. Schmauch, H. Roesner, Y. Ivanisenko, and J. Weissmueller, "Deforming nanoporous metal: Role of lattice coherency," Acta Mater. **57**, 2665 (2009).
[21]S. V. Petegem, S. Brandstetter, and R. Maass, "On the microstructure of nanoporous gold: An x-ray diffraction study," Nano Lett. **9**, 1158–1163 (2009).
[22]Z. H. Zhang, Y. Wang, Z. Qi, W. H. Zhang, J. Y. Qin, and J. Frenzel, "Generalized fabrication of nanoporous metals (Au, Pd, Pt, Ag, and Cu) through chemical dealloying," J. Phys. Chem. C **113**, 12629–12636 (2009).
[23]Y. F. Wang and A. S. Hall, "Room-temperature synthesis of intermetallic Cu–Zn by an electrochemically induced phase transformation," Chem. Mater. **33**, 7309 (2021).
[24]T. Song, M. Yan, N. A. S. Webster *et al.*, "*In-situ* and *ex-situ* synchrotron x-ray diffraction studies of microstructural length scale controlled dealloying," Acta Mater. **168**, 376–392 (2019).
[25]Y. Xue, F. Scaglione, P. Rizzi, and L. Batterzzati, "High performance SERS on nanoporous gold substrates synthesized by chemical de-alloying a Au-based metallic glass," Appl. Surf. Sci. **426**, 1113–1120 (2017).
[26]R. Li, N. Wu, J. J. Lu, Y. Jin, X. B. Chen, and T. Zhang, "Formation and evolution of a nanoporous bimetallic Ag–Cu alloy produced by electrochemical dealloying of Mg-(Ag-Cu)-Y metallic glass," Corros. Sci. **119**, 23–32 (2017).
[27]F. Scaglione, E. M. Paschalidou, P. Rizzi *et al.*, "Nanoporous gold obtained from a metallic glass precursor used as substrate for surface-enhanced Raman scattering," Philos. Mag. Lett. **95**, 474–482 (2015).
[28]Y. Xue, F. Scaglione, P. Rizzi, and L. Batterzzati, "Improving the chemical de-alloying of amorphous Au alloys," Corros. Sci. **127**, 141–146 (2017).
[29]X. K. Luo, R. Li, L. Huang *et al.*, "Nucleation and growth of nanoporous copper ligaments during electrochemical dealloying of Mg-based metallic glasses," Corros. Sci. **67**, 100–108 (2013).
[30]E. M. Paschalidou, F. Celegato, F. Scaglione *et al.*, "The mechanism of generating nanoporous Au by de-alloying amorphous alloys," Acta Mater. **119**, 177–183 (2016).
[31]J. Yu, Y. Ding, C. Xu *et al.*, "Nanoporous metals by dealloying multicomponent metallic glasses," Chem. Mater. **20**, 4548–4550 (2008).
[32]P. Rizzi, F. Scaglione, and L. Battezzati, "Nanoporous gold by dealloying of anamorphous precursor," J. Alloys Compd. **586**, S117–S120 (2014).
[33]*Binary Alloy Phase Diagrams*, edited T. B. Massalski (ASM International, 1990).
[34]K. Sieradzki, N. Dimitrov, D. Movrin, C. McCall, N. Vasiljevic, and J. Erlebacher, "The dealloying critical potential," J. Electrochem. Soc. **149**, B370–B377 (2002).
[35]H. W. Pickering, "Characteristic features of alloy polarization curves," Corros. Sci. **23**, 1107–1120 (1983).
[36]A. Dursun, D. V. Pugh, and S. G. Corcoran, "A steady-state method for determining the dealloying critical potential," Electrochem. Solid State Lett. **6**, B32–B34 (2003).
[37]F. Liu and H. J. Jin, "Extrinsic parting limit for dealloying of Cu–Rh," J. Electrochem. Soc. **165**, C999–1006 (2018).
[38]B. E. Warren, *X-Ray Diffraction* (Dover Publications Inc., New York, 1990).
[39]M. P. Fewell and J. M. Priest, "High-order diffractometry of expanded austenite using synchrotron radiation," Surf. Coat. Technol. **202**, 1802–1815 (2008).
[40]B. K. Brink, K. Stahl, T. L. Christiansen *et al.*, "On the elusive crystal structure of expanded austenite," Scr. Mater. **131**, 59–62 (2017).
[41]M. R. Daymond, M. A. M. Bourke, R. B. Von Dreele *et al.*, "Use of Rietveld refinement for elastic macrostrain determination and for evaluation of plastic strain history from diffraction spectra," J. Appl. Phys. **82**, 1554–1562 (1997).
[42]P. W. Stephens, "Phenomenological model of anisotropic peak broadening in powder diffraction," J. Appl. Crystallogr. **32**, 281–289 (1999).
[43]J. Weißmüller and J. W. Cahn, "Mean stresses in microstructures due to interface stresses: A generalization of a capillary equation for solids," Acta Mater. **45**, 1899–1906 (1997).
[44]X. L. Ye, N. Fortunato, A. Sarkar *et al.*, "Creating a ferromagnetic ground state with Tc above room temperature in a paramagnetic alloy through non-equilibrium nano-structuring," Adv. Mater. **34**, 2108793 (2022).
[45]H. J. Jin, X. L. Wang, S. Parida *et al.*, "Nanoporous Au–Pt alloys as large strain electrochemical actuators," Nano Lett. **10**, 187–194 (2010).
[46]G. Filoti, V. Kuncser, E. Navarro, A. Hernando, and M. Rosenberg, "Hyperfine fields and Fe magnetic moments in Fe–Rh alloys: A Mössbauer study," J. Alloy Compd. **278**, 60–68 (1998).
[47]V. Kuncser, M. Rosenberg, G. Principi, U. Russo, A. Hernando, E. Navarro, and G. Filoti, "Magnetic interactions in nanocrystalline FeRh alloys studied by in field Mössbauer spectroscopy," J. Alloys Compd. **308**, 21–29 (2000).
[48]P. Alippi, P. M. Marcus, and M. Scheffler, "Strained tetragonal states and Bain paths in metals," Phys. Rev. Lett. **78**, 3892 (1997).